CRYSTAL Research&Technology
www.crt-journal.org

# Stimulated Raman Scattering in Melilite-Type Crystals $Ca_2MgSi_2O_7$ and $Ca_2Ga_2SiO_7$

*Alexander A. Kaminskii, Ladislav Bohatý, Hans Joachim Eichler, Oliver Lux, Hanjo Rhee, Manfred Burianek, and Petra Becker**

**$\chi^{(3)}$-nonlinear optical interactions in two melilite-type stimulated Raman scattering (SRS)-active non-centrosymmetric crystals, $Ca_2MgSi_2O_7$ and $Ca_2Ga_2SiO_7$, formerly known as $Nd^{3+}$-laser media, are presented. Under picosecond pumping at 1.064 and 0.532 μm cascaded and cross-cascaded effects occur in these tetragonal silicates. Besides the SRS-promoting phonon modes with energy of $\omega_{SRS1} \approx 908$ cm$^{-1}$ and $\omega_{SRS2} \approx 668$ cm$^{-1}$ for $Ca_2MgSi_2O_7$, and $\omega_{SRS1} \approx 720$ cm$^{-1}$ and $\omega_{SRS2} \approx 550$ cm$^{-1}$ for $Ca_2Ga_2SiO_7$, respectively, combined phonon modes are observed. For $Ca_2MgSi_2O_7$ new data in a broad wavelength range of refractive indices and their dispersion are given as well. The observed $\chi^{(3)}$-nonlinear properties expand the functionality of the studied silicates and foreshadow their use in self-frequency Raman laser converters (self-SRS lasers).**

## 1. Introduction

Among the modern trends in the development of the physics of laser crystals the identification of new physical properties of these crystals, which can enrich their application potential, is of topical interest. In recent years, these trends were supported by fundamental studies of the numerous manifestations of nonlinear cascaded interactions in $\chi^{(3)}$- and $\chi^{(2)}+\chi^{(3)}$-active laser crystals doped with trivalent lanthanide ($Ln^{3+}$) lasant ions. Among them are crystals with melilite-type structure, with a history that dates back to 1968, when $Ba_2MgGe_2O_7$ was first described as a laser crystal.[1] In the following 50 years, a large number of melilite-type laser crystals have been discovered and investigated (see, e.g., reviews by Weber[2] and Kaminskii[3]). A new stage in the study of the physical properties of this class of crystals was marked in 2008, when the $\chi^{(3)}$-nonlinear effect of stimulated Raman scattering (SRS) was discovered just in the same laser "melilite" $Ba_2MgGe_2O_7$.[4] Over the past decade, $\chi^{(3)}$-nonlinear optical properties of a number of tetragonal (space group $P\bar{4}2m - D^3_{2d}$) "melilite" laser crystals have been discovered (see **Table 1**), giving them the status of SRS-active $Ln^{3+}$-laser crystals with enhanced application potential. Here, the realization of self-SRS-laser converters (also known as self-Raman lasers), where stimulated emission (SE) of the $Ln^{3+}$-ions is coherently converted into Stokes laser output radiation by SRS in the host crystal, offers the generation of new laser wavelengths and is thus of high interest.

The brief compilation of melilite-type $\chi^{(3)}$-nonlinear crystals given in Table 1 also provides an overview of observed $\chi^{(3)}$- and $\chi^{(2)}+\chi^{(3)}$-nonlinear photon–phonon processes. As follows from this table, non-centrosymmetric melilite-type crystals show diverse nonlinear optical properties and many of them are also laser-active media. The combination of these unique functional potentials allows for the creation of novel self-frequency conversion lasers. This prospect has motivated the present search for new SRS-active melilite-type crystals. For the melilite-type crystal $Ca_2MgSi_2O_7$, doped with $Nd^{3+}$ (and codoped with $Na^+$), laser activity was investigated in ref. [19] and in a recent short communication[21] the SRS potential of the (undoped) crystal was preliminarily demonstrated.

In the present work, linear optical properties and a detailed investigation of $\chi^{(3)}$-nonlinear optical properties of $Ca_2MgSi_2O_7$ are reported, together with SRS properties of a further melilite-type crystal, $Ca_2Ga_2SiO_7$.

Prof. A. A. Kaminskii[+]
Institute of Crystallography
Federal Scientific Center "Crystallography and Photonics,"
Russian Academy of Sciences
Moscow 119333, Russia

Prof. L. Bohatý, Dr. M. Burianek, Prof. P. Becker
Section Crystallography
Institute of Geology und Mineralogy
University of Cologne
Zülpicher Str. 49 b, Köln 50674, Germany
E-mail: petra.becker@uni-koeln.de

Prof. H. J. Eichler, Dr. O. Lux, Dr. H. Rhee
Institute of Optics and Atomic Physics
Technical University of Berlin
Berlin 10623, Germany

Dr. O. Lux
Institute of Atmospheric Physics
German Aerospace Center (DLR)
Münchener Str. 20, Oberpfaffenhofen, Wessling 82234, Germany

Dr. M. Burianek
Faculty Geosciences
University Bremen
Klagenfurter Straße 2-4, Bremen 28359, Germany

The ORCID identification number(s) for the author(s) of this article can be found under https://doi.org/10.1002/crat.202000038

[+]The author passed away during the preparation of the publication.



**DOI: 10.1002/crat.202000038**

**Table 1.** Known SRS- and $Ln^{3+}$-laser active tetragonal (space group $P\bar{4}2m - D_{2d}^3$) melilite-type crystals.

| Crystal | Observed $\chi^{(3)}$- and $\chi^{(2)}+\chi^{(3)}$-nonlinear optical interactions | SRS-promoting vibrational modes[a] [$cm^{-1}$] | Known SE-channels of $Ln^{3+}$-lasant ions |
|---|---|---|---|
| $Ba_2MgGe_2O_7$ | SRS, SHG,[b] THG,[c] "conical SHG,"[d] self-SHG(SRS),[e] SFG,[f] self-SFG(SHG),[g] $\chi^{(3)}$-comb,[h] self-SRS(SFG),[i] self-SFG(SHG,SRS),[j],[4] | 771.5[4] | ($Nd^{3+}$): $^4F_{3/2}\rightarrow{}^4I_{11/2}$ [1] |
| $Sr_2MgGe_2O_7$ | SRS, SHG, THG, $\chi^{(3)}$-comb, SFG, self-SFG(SHG), self-SFG(SHG,SRS)[5] | ≈779[5] | |
| $Sr_2ZnGe_2O_7$ | SRS, SHG, THG, $\chi^{(3)}$-comb, SFG, self-SFG(SHG), self-SFG(SHG,SRS)[6] | ≈778[6] | |
| $Ba_2ZnGe_2O_7$ | SRS, SHG, THG, $\chi^{(3)}$-comb, SFG, self-SHG(SRS), self-SRS(SHG), $\chi^{(3)}$-cr-casc[k],[5] | ≈778, ≈257[5] | ($Nd^{3+}$): $^4F_{3/2}\rightarrow{}^4I_{11/2}$[7,8] |
| $Ca_2ZnSi_2O_7$ | SRS, SHG, THG, $\chi^{(3)}$-comb, self-SFG(SRS), $\chi^{(3)}$-cr-casc[9] | ≈906, ≈663, ≈614, ≈243C[9] | |
| $SrLaGa_3O_7$ | SRS[10] | ≈523[10] | ($Nd^{3+}$): $^4F_{3/2}\rightarrow{}^4I_{11/2}$;[11] ($Pr^{3+}$): $^3P_0\rightarrow{}^3H_4$, $^3P_0\rightarrow{}^3F_2$[12] |
| $SrGdGa_3O_7$ | SRS[10] | ≈523, ≈225[10] | ($Nd^{3+}$): $^4F_{3/2}\rightarrow{}^4I_{9/2}$[13] |
| $Ca_2Ga_2SiO_7$ | SRS,[l] self-SFG(SRS),[m] $\chi^{(3)}$-comb, $\chi^{(3)}$-cr-casc (this work) | ≈720, ≈550, ≈170C, ≈1270C | ($Nd^{3+}$): $^4F_{3/2}\rightarrow{}^4I_{11/2}$,[14–18] $^4F_{3/2}\rightarrow{}^4I_{13/2}$[14,15] |
| $Ca_2MgSi_2O_7$ | SRS,[n] self-SFG(SRS), $\chi^{(3)}$-comb, $\chi^{(3)}$-cr-casc (this work) | ≈908, ≈668, ≈240C, ≈1576C | ($Nd^{3+}$): $^4F_{3/2}\rightarrow{}^4I_{11/2}$[19] |

[a] The character "C" denotes combined SRS-active vibrational modes [b] SHG: Second harmonic generation [c] THG: Third harmonic generation [d] "Conical SHG": Conical harmonic generation, see, e.g., ref. [20] [e] Self-SHG(SRS): Self-frequency doubling, i.e., SHG of the (anti-)Stokes components [f] SFG: Sum-frequency generation (mixing) [g] Self-SFG(SHG): Sum-frequency generation involving SHG and SRS components [h] $\chi^{(3)}$-comb: a frequency comb consisting of Stokes and anti-Stokes components that span at least one octave, i.e., the highest frequency (energy) component must be at least double of the lowest frequency component [i] Self-SRS(SFG): SRS originated from intense SFG of the pump wave and (anti-)Stokes components [j] Self-SFG(SHG,SRS): Sum-frequency generation involving SHG and (anti-)Stokes components [k] $\chi^{(3)}$-cr-casc: Cascade of one or many-step $\chi^{(3)}$-processes involving different SRS-active vibrational modes of the crystal for the generation of high-order Stokes and anti-Stokes components [l] Preliminary information on SRS is given in ref. [9] [m] Self-SFG(SRS): Sum-frequency generation involving the pump radiation and its (anti-)Stokes components [n] Preliminary information on SRS is given in ref. [21].

## 2. Crystals of $Ca_2Ga_2SiO_7$ and $Ca_2MgSi_2O_7$ and Linear Optical Properties

The parent crystal structure of melilite-type crystals with an overall chemical composition $M_2T^{(1)}T_2^{(2)}O_7$, which can host a multitude of tetrahedrally coordinated ($T^{(1)}$ and $T^{(2)}$) and eightfold coordinated (M) cations, crystallizes with tetragonal space group symmetry $P\bar{4}2m - D_{2d}^3$ (for an overview see, e.g., refs. [4,22,23]). The structure consists of corner-sharing double-tetrahedra [$T_2^{(2)}O_7$] and single tetrahedra [$T^{(1)}O_4$] that form layers parallel to (001). These layers alternate with layers of the eightfold coordinated M cations.[24] This parent melilite-type crystal structure is adopted by $Ca_2Ga_2SiO_7$, where Ga occupies the tetrahedrally coordinated $T^{(1)}$ position, while the $T^{(2)}$ position is shared among Ga and Si with an occupation factor of 0.5 for both kinds of atoms. The M position is occupied by Ca.[14] The parent ("normal," N) melilite-type structure is also found for $Ca_2MgSi_2O_7$ at temperatures above ≈355 K (high temperature phase at ambient pressure), with tetrahedrally coordinated Mg and Si on positions $T^{(1)}$ and $T^{(2)}$, respectively, and Ca occupying the M position.[25] Below ≈355 K $Ca_2MgSi_2O_7$ shows a 2D incommensurately modulated (IC) structure with modulation vectors $q_1 = \beta(a^* + b^*)$ and $q_2 = \beta(-a^* + b^*)$ (with $a^*$, $b^*$ = tetragonal reciprocal axes of the basic unit cell, and $\beta$ = temperature-dependent component of the modulation vectors),[26,27] which, after,[27] origins in a misfit between the layers of $T^{(1)}O_4 + T_2^{(2)}O_7$ groups and the layers of $Ca^{2+}$ cations and cause a slight distortion and rotation of the tetrahedral structural units and a distortion of the Ca coordination surrounding.[27] The structure of IC-$Ca_2MgSi_2O_6$ can be described with a 5D model with the superspace group $P\bar{4}2_1m : p4mg$.[25,28,29]

Crystals of $Ca_2Ga_2SiO_7$ had been grown by the Czochralski technique at ≈1738 K from stoichiometric melt in a weakly oxidizing atmosphere as described in ref. [17]. The crystals

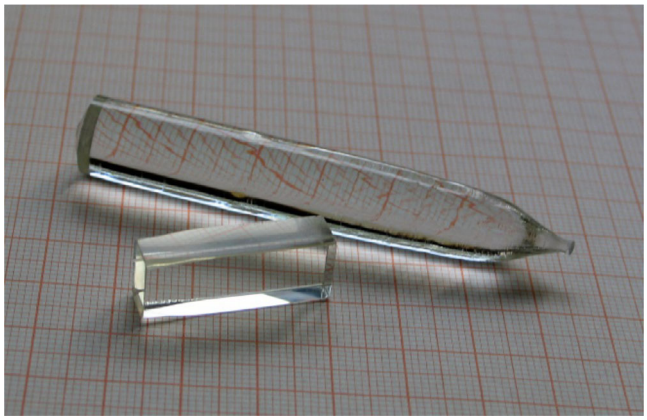

**Figure 1.** Example of a grown crystal of $Ca_2MgSi_2O_6$, together with one of the prepared oriented samples for the SRS investigations in the present work.

of $Ca_2MgSi_2O_7$ used in the present work were grown by the Czochralski technique from a melt with a slight surplus of 1 wt% MgO and of 3 wt% $SiO_2$ in order to avoid the formation of $Ca_3MgSi_2O_8$ as a parasitic phase during the growth process (as reported in ref. [37]). Growth was performed at ≈1703 K in air using seed crystal orientation along [001], Pt crucibles, crystal pulling rate of 1–1.5 mm $h^{-1}$ and crystal rotation of 20–30 rpm. Applying a rather flat temperature gradient of less than 20 K $cm^{-1}$ large single crystals of optical quality and dimensions up to 70 mm length and 15 mm diameter were obtained, see **Figure 1**.

For SRS investigations two parallel-epipedal samples with face normals along the tetragonal axes *a*, *b*, *c* and dimensions 9.92 × 6.99 × 27.10 $mm^3$ (sample I, see Figure 1) and 8.66 × 7.86 × 18.60 $mm^3$ (sample II) were prepared for $Ca_2MgSi_2O_7$, and one sample of the same orientation with dimensions 9.0 × 10.4 × 11.5 $mm^3$ for $Ca_2Ga_2SiO_7$. For all samples, the sample faces were polished but without antireflection coating.

Using a plate-shaped sample with faces {001} of $Ca_2MgSi_2O_7$ of 0.79 mm thickness the optical transparency range was measured with a Perkin Elmer Lambda 19 UV/vis/NIR spectrophotometer. The UV transmission border (at 50% transmission level) is at ≈0.25 µm, the IR transmission range exceeds the IR wavelength range accessible with our equipment and thus is higher than 3.2 µm, see **Figure 2**.

While refractive indices and their wavelength dispersion of $Ca_2Ga_2SiO_7$ in the wavelength range 0.308–1.064 µm are reported in literature[30] (see also **Table 2**), refractive indices of $Ca_2MgSi_2O_7$ are given in literature only in the wavelength range of visible light.[31,32] Therefore, we determined the refractive indices and their wavelength dispersion of $Ca_2MgSi_2O_7$ in a broad wavelength range between 0.36502 and 2.32531 µm. The measurement of the refractive indices was performed by the prism method using a prism with refracting edge [001] and faces (hk0), and a high-precision goniometer-spectrometer system

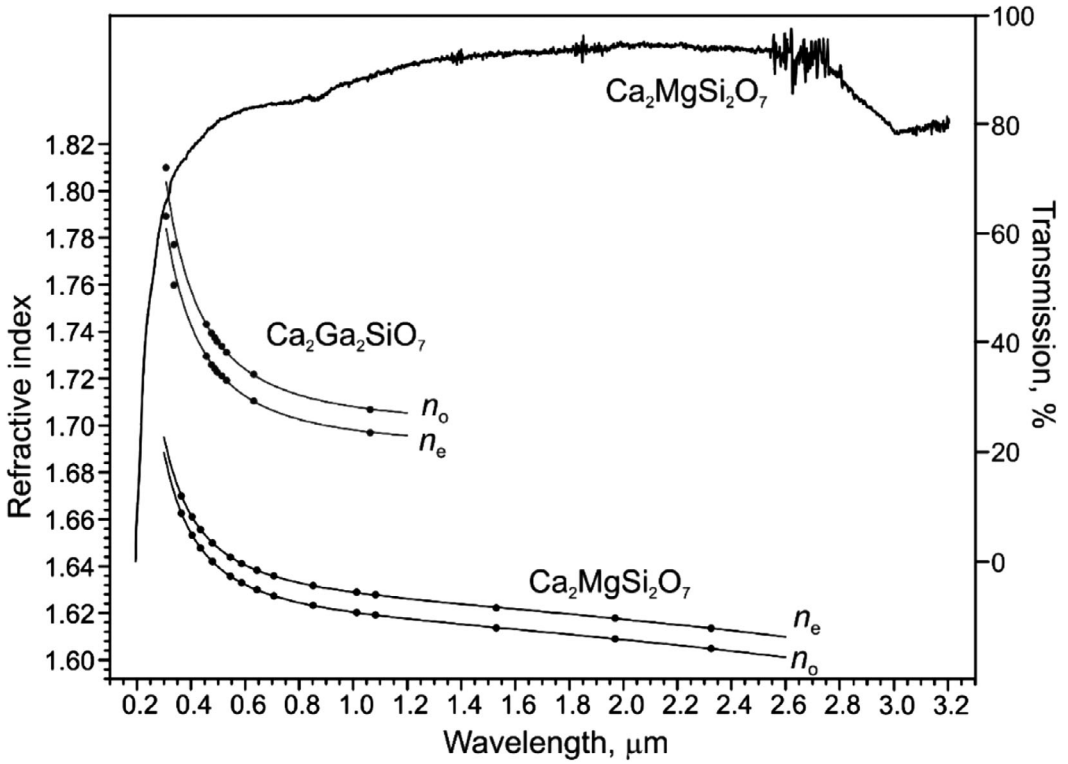


**Figure 2.** Measured transmission spectrum (refers to the right axis) and refractive indices and their wavelength dispersion (left axis) of uniaxial positive $Ca_2MgSi_2O_7$. Refractive indices were measured by the prism method. Dots represent measured and corrected (see text) data, lines give the Sellmeier fits of the data. Error bars of the measured data are smaller than the data markers. Refractive indices of uniaxial negative $Ca_2Ga_2SiO_7$, taken from ref. [30], are given in comparison, together with the Sellmeier fit curves (lines) given in ref. [30], see also Table 2.

**Table 2.** Selected crystallographic and physical properties of $Ca_2MgSi_2O_7$ and $Ca_2Ga_2SiO_7$ silicate crystals.

| Characteristics | $Ca_2MgSi_2O_7$ | $Ca_2Ga_2SiO_7$ |
|---|---|---|
| Space group[25] | $P\bar{4}2m$ – $D^3_{2d}$ (No. 113)[a] | |
| Unit cell parameters [Å] | $a = b = 7.8348(3)$; $c = 5.0087(2)$[25] | $a = b = 7.793(3)$; $c = 5.132(2)$[14] |
| Formula unit per unit cell | $Z = 2$[25] | |
| Melting temperature [K] | ≈1727[35] | ≈1738[14] |
| Method of crystal growth | Czochralski[15,19,36,37] | |
| Hardness (Mohs scale) | 5–6[38] | |
| Density [g cm$^{-3}$] | 2.945[25] | 3.828[14] |
| Nonlinearities | $\chi^{(2)} + \chi^{(3)}$ | |
| Linear optical character | Uniaxial positive ($n_o < n_e$)[31] | Uniaxial negative ($n_o > n_e$)[17] |
| Refractive index (modified Sellmeier equations) | $n^2(\lambda) = D_1 + \frac{D_2}{(\lambda^2 - D_3)} - D_4\lambda^2$[b] | $n^2(\lambda) = 1 + \frac{A\cdot\lambda^2}{(\lambda^2 - B^2)}$[c],[30] |
| Nonlinear refractive index [m$^2$ W$^{-1}$] | | $n_2 = (6.5 \pm 1) \times 10^{-20}$[39] |
| Phonon spectra extension[d] [cm$^{-1}$] | ≈1030[46] | ≈720[14] |
| Observed SRS-promoting vibrational modes[e] [cm$^{-1}$] | $\omega_{SRS1} \approx 908$; $\omega_{SRS2} \approx 668$; $\omega_{SRS3C} \approx 240$; $\omega_{SRS4C} \approx 1576$ | $\omega_{SRS1} \approx 720$; $\omega_{SRS2} \approx 550$; $\omega_{SRS3C} \approx 170$; $\omega_{SRS4C} \approx 1270$ |

[a] $Ca_2MgSi_2O_7$ crystals possess an incommensurate–commensurate phase transition at ≈355 K,[26,27] see text [b] Sellmeier coefficients ($\lambda$ in µm; $\xi^2$ is the sum of the squares of the residuals):

| | $D_1$ | $D_2$ | $D_3$ | $D_4$ | $\xi^2$ |
|---|---|---|---|---|---|
| $n_o$ | 2.6159(3) | 0.0176(2) | 0.0154(10) | 0.00810(9) | $7.8 \times 10^{-9}$ |
| $n_e$ | 2.6440(4) | 0.0173(2) | 0.0150(14) | 0.00810(11) | $1.4 \times 10^{-8}$ |

[c] Sellmeier coefficients for $n_o$ and $n_e$ ($\lambda$ in µm): $A_o = 1.8879(6)$, $B^2_o = 0.015389(5)$ (µm$^2$), $A_e = 1.8570(7)$, $B^2_e = 0.014139(6)$ (µm$^2$)[30] [d] Data taken from room-temperature spontaneous Raman scattering spectra [e] The letter "C" denotes combined SRS-active vibrational modes.

(Möller-Wedel, for instrumental details see, e.g., ref. [33]). Refractive indices were measured at 14 discrete wavelength and the measured data were corrected with the refractive index of air using the Edlén equation and data for air given in ref. [34]. The corrected refractive indices for $n_o$ and $n_e$ were fitted with a modified Sellmeier equation (see Table 2). In Figure 2, the (corrected) refractive index data are given, together with the Sellmeier fits, the Sellmeier parameters are listed in footnote b of Table 2. The latter also contains selected further known relevant crystallographic and physical properties of the two melilite-type crystals. In Figure 2, the refractive indices and the Sellmeier fit curves of $Ca_2Ga_2SiO_7$ given in ref. [30] are included for comparison as well.

Based on the refractive indices and their dispersion phase matching possibilities for collinear SHG were calculated using a well-tested home-made program. Both melilite-type crystals, $Ca_2MgSi_2O_7$ and $Ca_2Ga_2SiO_7$, do not allow collinear SHG phase matching between their UV absorption edge and 3.5 µm.

## 3. $\chi^{(3)}$ Nonlinear Lasing

The spectroscopic investigation of $\chi^{(3)}$-nonlinear optical processes in $Ca_2MgSi_2O_7$ and $Ca_2Ga_2SiO_7$ single crystals was performed using a mode-locked $Nd^{3+}$:$Y_3Al_5O_{12}$ master oscillator power amplifier system in combination with a spectrometric setup, as described in previous publications (see, e.g., refs. [40,41]). The pump laser system operated at 1 Hz repetition rate, generating single pulses at $\lambda_{f1}$ = 1.06415 µm wavelength with pulse energy of up to 40 mJ and pulse duration of about 80 ps. The pump beam was guided to the registration part of the experimental setup which is shown in **Figure 3**a.

After propagation through an attenuation stage consisting of a revolving half-wave-plate ($\lambda_{f1}/2$) in combination with a Glan-laser polarizer (P), the linearly polarized and collimated pump beam could optionally be frequency-doubled using a $KTiOPO_4$ (KTP) crystal. The SHG process generated ≈60 ps pulses at $\lambda_{f2}$ = 0.53207 µm wavelength. Suppression of the residual infrared radiation was accomplished by inserting a Schott BG39 filter glass behind the KTP crystal, which shows a transmission of 0.015% at 1.06415 µm and 96% at 0.53207 µm wavelength. The nearly Gaussian beam was then focused into the melilite crystal by using a plano-convex lens with a focal length of $f_{L1}$ = 250 mm. A lens system consisting of a spherical bi-convex lens ($f_{L2}$ = 100 mm) and a plano-convex cylindrical lens ($f_{L3}$ = 100 mm) collimated the divergent output radiation and imaged it onto the variable entrance slit of a Czerny-Turner monochromator (McPherson Model 270, 6.8 Å pixel$^{-1}$ dispersion, 150 lines mm$^{-1}$ grating). The spectral composition of the scattered emission was finally recorded by a silicon CCD sensor (Hamamatsu S3924-1024Q with 1024 pixels) for the UV and visible spectral region and an InGaAs-CMOS sensor (Hamamatsu G9204-512D with 512 pixels) for the range between 0.9 and 1.7 µm, respectively (see spectral sensitivity of the two detectors in Figure 3b).

For both crystals, $Ca_2MgSi_2O_7$ and $Ca_2Ga_2SiO_7$, SRS measurements were performed using three different excitation geometries, namely, *a*(*cc*)*a*, *c*(*aa*)*c*, and *b*(*aa*)*b* (notation used in analogy to that in ref. [42], see also footnote a of **Table 3**). SRS and Raman-induced four-wave mixing (RFWM) spectra obtained for $Ca_2MgSi_2O_7$ with pump wave of $\lambda_{f2}$ = 0.53207 µm are shown in **Figures 4–6**. In addition, pumping at $\lambda_{f1}$ = 1.06415 µm was applied for *a*(*cc*)*a* and *c*(*aa*)*c* geometries (see **Figures 7** and **8**) and for *b*(*aa*)*b* geometry in Figure 5b. The analysis of the observed spectra is given in Table 3. For $Ca_2Ga_2SiO_7$ a pump wave with $\lambda_{f2}$ = 0.53207 µm was applied exclusively. The resulting SRS and RFWM spectra are visualized in **Figure 9**a for geometry *b*(*aa*)*b*, Figure 9b for geometry *a*(*cc*)*a*, and **Figure 10** for excitation geometry *c*(*aa*)*c*. Their analysis is listed in Table 3.

The analysis of the SRS and RFWM spectra of the tetragonal melilite-type silicate crystals revealed a number of $\chi^{(3)}$-nonlinear optical cascaded and cross-cascaded processes, which are related to two original vibrational modes with energies of $\omega_{SRS1} \approx 908$ cm$^{-1}$ and $\omega_{SRS2} \approx 668$ cm$^{-1}$ for $Ca_2MgSi_2O_7$. These modes correspond to the strongest lines in the spontaneous Raman scattering spectrum.[46] For $Ca_2Ga_2SiO_7$ the two original vibrational modes have energies $\omega_{SRS1} \approx 720$ cm$^{-1}$ and $\omega_{SRS2} \approx 550$ cm$^{-1}$, respectively, and, analogously, correspond to pronounced

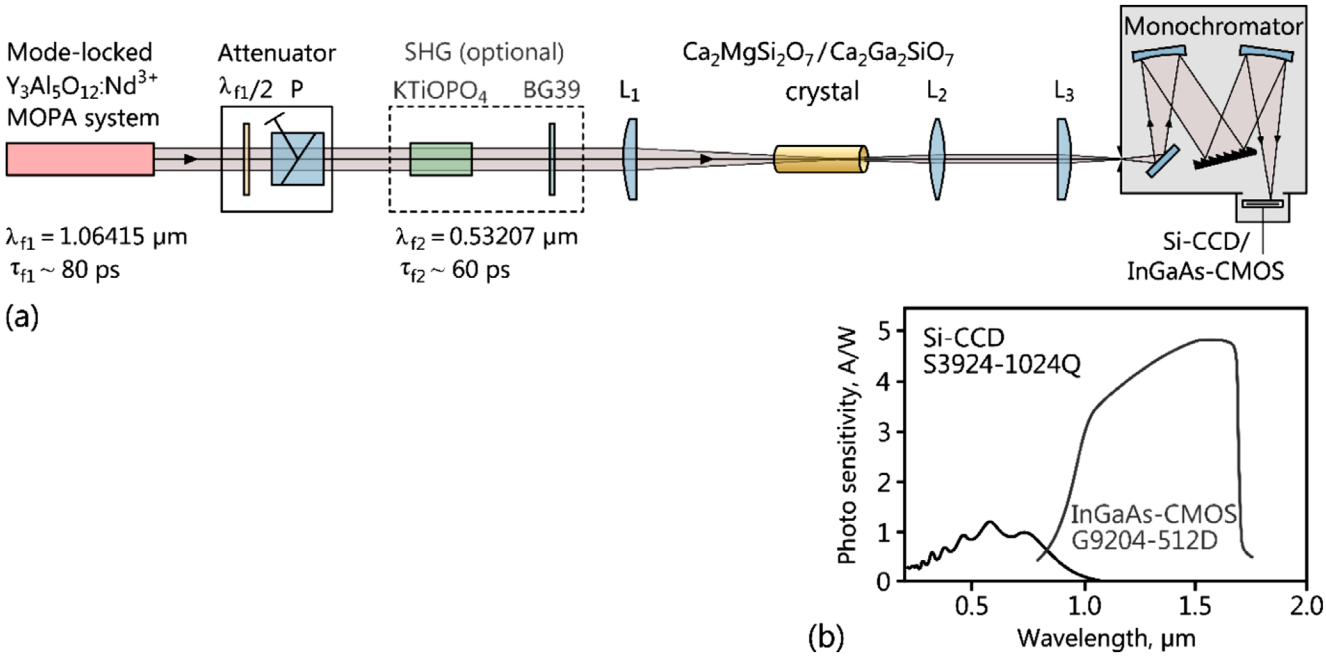


**Figure 3.** a) Schematic diagram of the experimental setup used for the spectroscopic analysis of SRS and nonlinear mixing interactions in $Ca_2MgSi_2O_7$ or $Ca_2Ga_2SiO_7$ single crystals (P: polarizer; $L_1$–$L_3$: lenses; see also text). b) Spectral sensitivity of the used Si-CCD and an InGaAs-CMOS line sensor (data are taken from Hamamatsu Photonics K.K. technical data sheets).

lines of the spontaneous Raman spectrum.[14] As shown in Figures 5 and 7, for $Ca_2MgSi_2O_7$ pumping with incidence perpendicular to the optic axis of the crystal allows the separation of the SRS-active vibration modes and, for both modes, broadband Stokes and anti-Stokes comb generation via SRS and RFWM. This mode separation is also observed for SRS in $Ca_2Ga_2SiO_7$ and is demonstrated in Figure 9. Pumping with incidence along the optic axis of the tetragonal crystals results in activation of both SRS-promoting modes $\omega_{SRS1}$ and $\omega_{SRS2}$ with the emergence of cross-cascaded $\chi^{(3)}$-nonlinear transitions and, in addition, the occurrence of two SRS-active "combined modes," see Figures 6 and 8 for $Ca_2MgSi_2O_7$ and Figure 10 for $Ca_2Ga_2SiO_7$, see also Table 3. As explained in footnote e of Table 3, the "combined" vibrational modes with energies $\omega_{SRS3C} \approx 240$ cm$^{-1}$ and $\omega_{SRS4C} \approx 1576$ cm$^{-1}$ for $Ca_2MgSi_2O_7$, respectively, $\omega_{SRS3C} \approx 170$ cm$^{-1}$ and $\omega_{SRS4C} \approx 1270$ cm$^{-1}$ for $Ca_2Ga_2SiO_7$, are absent from the respective spontaneous Raman scattering spectrum, as they result from $\chi^{(3)}$-nonlinear coherent interaction of the two modes $\omega_{SRS1} \approx 908$ cm$^{-1}$ and $\omega_{SRS2} \approx 668$ cm$^{-1}$ (for $Ca_2MgSi_2O_7$), and $\omega_{SRS1} \approx 720$ cm$^{-1}$ and $\omega_{SRS2} \approx 550$ cm$^{-1}$ (for $Ca_2Ga_2SiO_7$), respectively.

The vibrational nature of the modes of the studied melilite-type silicates can be derived based on investigations of the spontaneous Raman scattering spectra of several melilite-type silicates (see, e.g., refs. [9,46]). Their tetragonal ($P\bar{4}2m - D_{2d}^3$) unit cell comprises 24 atoms that have 72 zone-center degrees of freedom, which characterize the lattice vibrations as follows: $\Gamma_{72} = 10A_1+6A_2+7B_1+11B_2+19E$. Among them the 69 phonons $\Gamma_O = 10A_1+6A_2+7B_1+10B_2+18E$ correspond to the optical modes. The unit cells of the studied crystals contain two $Si_2O_7$ units ($Ca_2MgSi_2O_7$), resp. two $T_2^{(2)}O_7$ units ($Ca_2Ga_2SiO_7$, with $T^{(2)}$ = Si, Ga). An analysis[46] shows for $Ca_2MgSi_2O_7$ that the observed SRS spectral lines are related to fully symmetric $A_1$ optical modes involving three oxygen atoms and one silicon atom. The lines at ≈908 cm$^{-1}$ and at ≈668 cm$^{-1}$ for $Ca_2MgSi_2O_7$ can be assigned to the $\nu_s(SiO_3)$ and to the $\nu_s(SiOSi)$ vibrations ($A_1$-modes), respectively. Shift dynamics of the atoms of these modes are explained by the atomic displacement vectors of these phonons, which have been studied in ref. [46] (see Table 3 therein). An assignment of the lines at ≈720 cm$^{-1}$ and at ≈550 cm$^{-1}$ for $Ca_2Ga_2SiO_7$ (see also ref. [14]) in analogy to that for $Ca_2MgSi_2O_7$ gives the $\nu_s(T^{(2)}O_3)$ and the $\nu_s(T^{(2)}OT^{(2)})$ vibrations ($A_1$-modes; $T^{(2)}$ = Si, Ga), respectively.

## 4. Discussion

The comparison of the linear optical properties of $Ca_2MgSi_2O_7$ with those of further melilite-type crystals[33,47] shows that the properties of $Ca_2MgSi_2O_7$ fit well into the earlier observed tendencies of the influence of cation substitution in the melilite-type structure on $\chi^{(1)}$ optical properties.[47] Here, particularly the influence on the birefringence of the crystals and thus on phase matching for $\chi^{(2)}$-processes is of interest. A variation of the eightfold coordinated M-site occupation of the melilite-type structure in a series Ba→Sr→Ca leads to a general reduction of birefringence, as well as the $T^{(1)}$-site substitution Mg↔Zn, which affects optical birefringence in a pronounced way with frequently larger birefringence for the Mg compounds (with

**Table 3.** Spectral composition of SRS and RFWM generation as well as of cascaded and cross-cascaded $\chi^{(3)} \leftrightarrow \chi^{(3)}$ nonlinear lasing in $Ca_2MgSi_2O_7$ and $Ca_2Ga_2SiO_7$ crystals, recorded at room temperature with picoseconds $Nd^{3+}$:$Y_3Al_5O_{12}$-laser pumping at fundamental wavelengths $\lambda_{f1}$ = 1.06415 μm and $\lambda_{f2}$ = 0.53207 μm (SHG).

| Pumping condition | $\chi^{(3)}$-nonlinear lasing components | | | | SRS-promoting vibration modes [$cm^{-1}$] | | | |
|---|---|---|---|---|---|---|---|---|
| $\lambda_f$ [μm] | Excitation geometry[a] | Wave-length[b] [μm] | Spectral line[c] | Attribution[d] | $\omega_{SRS1}$ | $\omega_{SRS2}$ | $\omega_{SRS3}$[e] | $\omega_{SRS4}$[e] |
| $Ca_2MgSi_2O_7$ crystal | | | | | | | | |
| 0.53207 | *a*(*cc*)*a* (see Figure 4) | 0.4647 | $ASt_{3\text{-}1}$ | $*\omega_{f2}+3\omega_{SRS1}=\omega_{ASt3\text{-}1}$ | ≈908 | | | |
| | | 0.4852 | $ASt_{2\text{-}1}$ | $*\omega_{f2}+2\omega_{SRS1}=\omega_{ASt2\text{-}1}$ | ≈908 | | | |
| | | 0.5076 | $ASt_{1\text{-}1}$ | $*\omega_{f2}+\omega_{SRS1}=\omega_{ASt1\text{-}1}$ | ≈908 | | | |
| | | 0.53207 | $\lambda_{f2}$ | $\omega_{f2}$ | – | | | |
| | | 0.5591 | $St_{1\text{-}1}$ | $\omega_{f2}-\omega_{SRS1}=\omega_{St1\text{-}1}$ | ≈908 | | | |
| | | 0.5890 | $St_{2\text{-}1}$ | $*\omega_{f2}-2\omega_{SRS1}=\omega_{St2\text{-}1}$ | ≈908 | | | |
| | | 0.6228 | $St_{3\text{-}1}$ | $*\omega_{f2}-3\omega_{SRS1}=\omega_{St3\text{-}1}$ | ≈908 | | | |
| | ≈*b*(*aa*)≈*b* (see Figure 5a) | 0.4518 | $ASt_{5\text{-}2}$ | $*\omega_{f2}+5\omega_{SRS2}=\omega_{ASt5\text{-}2}$ | | ≈668 | | |
| | | 0.4658 | $ASt_{4\text{-}2}$ | $*\omega_{f2}+4\omega_{SRS2}=\omega_{ASt4\text{-}2}$ | | ≈668 | | |
| | | 0.4808 | $ASt_{3\text{-}2}$ | $*\omega_{f2}+3\omega_{SRS2}=\omega_{ASt3\text{-}2}$ | | ≈668 | | |
| | | 0.4968 | $ASt_{2\text{-}2}$ | $*\omega_{f2}+2\omega_{SRS2}=\omega_{ASt2\text{-}2}$ | | ≈668 | | |
| | | 0.5138 | $ASt_{1\text{-}2}$ | $*\omega_{f2}+\omega_{SRS2}=\omega_{ASt1\text{-}2}$ | | ≈668 | | |
| | | 0.53207 | $\lambda_{f2}$ | $\omega_{f2}$ | – | | | |
| | | 0.5517 | $St_{1\text{-}2}$ | $\omega_{f2}-\omega_{SRS2}=\omega_{St1\text{-}2}$ | | ≈668 | | |
| | | 0.5728 | $St_{2\text{-}2}$ | $*\omega_{f2}-2\omega_{SRS2}=\omega_{St2\text{-}2}$ | | ≈668 | | |
| | | 0.5956 | $St_{3\text{-}2}$ | $*\omega_{f2}-3\omega_{SRS2}=\omega_{St3\text{-}2}$ | | ≈668 | | |
| | | 0.6202 | $St_{4\text{-}2}$ | $*\omega_{f2}-4\omega_{SRS2}=\omega_{St4\text{-}2}$ | | ≈668 | | |
| | *c*(*aa*)*c* (see Figure 6) | 0.4647 | $ASt_{3\text{-}1}$ | $*\omega_{f2}+3\omega_{SRS1}=\omega_{ASt3\text{-}1}$ | ≈908 | | | |
| | | 0.4852 | $ASt_{2\text{-}1}$ | $*\omega_{f2}+2\omega_{SRS1}=\omega_{ASt2\text{-}1}$ | ≈908 | | | |
| | | 0.4909 | $ASt_{1\text{-}4}$ | $**\omega_{f2}+\omega_{SRS4}=\omega_{ASt1\text{-}4}$ | | | | ≈1576 |
| | | 0.4968 | $ASt_{2\text{-}2}$ | $*\omega_{f2}+2\omega_{SRS2}=\omega_{ASt2\text{-}2}$ | | ≈668 | | |
| | | 0.5014 | $ASt_{1\text{-}3}\{ASt_{1\text{-}1}\}$ | $**[(\omega_{f2}+\omega_{SRS1})+\omega_{SRS3}]=$ $=\omega_{ASt1\text{-}3\{ASt1\text{-}1\}}$ | ≈908 | | ≈240 | |
| | | 0.5076 | $ASt_{1\text{-}1}$ | $*\omega_{f2}+\omega_{SRS1}=\omega_{ASt1\text{-}1}$ | ≈908 | | | |
| | | 0.5138 | $ASt_{1\text{-}2}$ | $*\omega_{f2}+\omega_{SRS2}=\omega_{ASt1\text{-}2}$ | | ≈668 | | |
| | | 0.5254 | $ASt_{1\text{-}3}$ | $**\omega_{f2}+\omega_{SRS3}=\omega_{ASt1\text{-}3}$ | | | ≈240 | |
| | | 0.53207 | $\lambda_{f2}$ | $\omega_{f2}$ | – | | | |
| | | 0.5390 | $St_{1\text{-}3}$ | $**\omega_{f2}-\omega_{SRS3}=\omega_{St1\text{-}3}$ | | | ≈240 | |
| | | 0.5517 | $St_{1\text{-}2}$ | $\omega_{f2}-\omega_{SRS2}=\omega_{St1\text{-}2}$ | | ≈668 | | |
| | | 0.5591 | $St_{1\text{-}1}$ | $\omega_{f2}-\omega_{SRS1}=\omega_{St1\text{-}1}$ | ≈908 | | | |
| | | 0.5667 | $St_{1\text{-}3}\{St_{1\text{-}1}\}$ | $**[(\omega_{f2}-\omega_{SRS1})-\omega_{SRS3}]=$ $=\omega_{St1\text{-}3\{St1\text{-}1\}}$ | ≈908 | | ≈240 | |
| | | 0.5728 | $St_{2\text{-}2}$ | $*\omega_{f2}-2\omega_{SRS2}=\omega_{St2\text{-}2}$ | | ≈668 | | |
| | | 0.5808 | $St_{1\text{-}4}$ | $**\omega_{f2}-\omega_{SRS4}=\omega_{St1\text{-}4}$ | | | | ≈1576 |
| | | 0.5890 | $St_{2\text{-}1}$ | $*\omega_{f2}-2\omega_{SRS1}=\omega_{St2\text{-}1}$ | ≈908 | | | |
| | | 0.6228 | $St_{3\text{-}1}$ | $*\omega_{f2}-3\omega_{SRS1}=\omega_{St3\text{-}1}$ | ≈908 | | | |
| 1.06415 | *a*(*cc*)*a* (see Figure 7) | 0.5692 | $ASt_{9\text{-}1}$ | $*\omega_{f1}+9\omega_{SRS1}=\omega_{ASt9\text{-}1}$ | ≈908 | | | |
| | | 0.6002 | $ASt_{8\text{-}1}$ | $*\omega_{f1}+8\omega_{SRS1}=\omega_{ASt8\text{-}1}$ | ≈908 | | | |
| | | 0.6348 | $ASt_{7\text{-}1}$ | $*\omega_{f1}+7\omega_{SRS1}=\omega_{ASt7\text{-}1}$ | ≈908 | | | |
| | | 0.6736 | $ASt_{6\text{-}1}$ | $*\omega_{f1}+6\omega_{SRS1}=\omega_{ASt6\text{-}1}$ | ≈908 | | | |
| | | 0.7175 | $ASt_{5\text{-}1}$ | $*\omega_{f1}+5\omega_{SRS1}=\omega_{ASt5\text{-}1}$ | ≈908 | | | |
| | | 0.7675 | $ASt_{4\text{-}1}$ | $*\omega_{f1}+4\omega_{SRS1}=\omega_{ASt4\text{-}1}$ | ≈908 | | | |
| | | 0.8250 | $ASt_{3\text{-}1}$ | $*\omega_{f1}+3\omega_{SRS1}=\omega_{ASt3\text{-}1}$ | ≈908 | | | |
| | | 0.8918 | $ASt_{2\text{-}1}$ | $*\omega_{f1}+2\omega_{SRS1}=\omega_{ASt2\text{-}1}$ | ≈908 | | | |
| | | 0.9385 | $Y_3Al_5O_{12}$:$Nd^{3+}$ | Luminescence[f] | | | | |
| | | 0.9460 | | | | | | |

(*Continued*)

**Table 3.** Continued.

| Pumping condition | $\chi^{(3)}$-nonlinear lasing components | | | | SRS-promoting vibration modes [$cm^{-1}$] | | | |
|---|---|---|---|---|---|---|---|---|
| $\lambda_f$ [μm] | Excitation geometry[a] | Wave-length[b] [μm] | Spectral line[c] | Attribution[d] | $\omega_{SRS1}$ | $\omega_{SRS2}$ | $\omega_{SRS3}$[e] | $\omega_{SRS4}$[e] |
| | | 0.9704 | $AST_{1\text{-}1}$ | $*\omega_{f1}+\omega_{SRS1}=\omega_{ASt1\text{-}1}$ | ≈908 | | | |
| | | 1.06415 | $\lambda_{f1}$ | $\omega_{f1}$ | – | | | |
| | | 1.1780 | $St_{1\text{-}1}$ | $\omega_{f1}-\omega_{SRS1}=\omega_{St1\text{-}1}$ | ≈908 | | | |
| | | 1.3191 | $St_{2\text{-}1}$ | $*\omega_{f1}-2\omega_{SRS1}=\omega_{St2\text{-}1}$ | ≈908 | | | |
| | | 1.4985 | $St_{2\text{-}1}$ | $*\omega_{f1}-3\omega_{SRS1}=\omega_{St3\text{-}1}$ | ≈908 | | | |
| | ≈*b*(*aa*)≈*b* (see Figure 5b) | 0.5531 | $AST_{13\text{-}2}$ | $*\omega_{f1}+13\omega_{SRS2}=\omega_{ASt13\text{-}2}$ | | ≈668 | | |
| | | 0.5743 | $AST_{12\text{-}2}$ | $*\omega_{f1}+12\omega_{SRS2}=\omega_{ASt12\text{-}2}$ | | ≈668 | | |
| | | 0.5972 | $AST_{11\text{-}2}$ | $*\omega_{f1}+11\omega_{SRS2}=\omega_{ASt11\text{-}2}$ | | ≈668 | | |
| | | 0.6220 | $AST_{10\text{-}2}$ | $*\omega_{f1}+10\omega_{SRS2}=\omega_{ASt10\text{-}2}$ | | ≈668 | | |
| | | 0.6490 | $AST_{9\text{-}2}$ | $*\omega_{f1}+9\omega_{SRS2}=\omega_{ASt9\text{-}2}$ | | ≈668 | | |
| | | 0.6784 | $AST_{8\text{-}2}$ | $*\omega_{f1}+8\omega_{SRS2}=\omega_{ASt8\text{-}2}$ | | ≈668 | | |
| | | 0.7106 | $AST_{7\text{-}2}$ | $*\omega_{f1}+7\omega_{SRS2}=\omega_{ASt7\text{-}2}$ | | ≈668 | | |
| | | 0.7460 | $AST_{6\text{-}2}$ | $*\omega_{f1}+6\omega_{SRS2}=\omega_{ASt6\text{-}2}$ | | ≈668 | | |
| | | 0.7851 | $AST_{5\text{-}2}$ | $*\omega_{f1}+5\omega_{SRS2}=\omega_{ASt5\text{-}2}$ | | ≈668 | | |
| | | 0.8286 | $AST_{4\text{-}2}$ | $*\omega_{f1}+4\omega_{SRS2}=\omega_{ASt4\text{-}2}$ | | ≈668 | | |
| | | 0.8771 | $AST_{3\text{-}2}$ | $*\omega_{f1}+3\omega_{SRS2}=\omega_{ASt3\text{-}2}$ | | ≈668 | | |
| | | 0.9317 | $AST_{2\text{-}2}$ | $*\omega_{f1}+2\omega_{SRS2}=\omega_{ASt2\text{-}2}$ | | ≈668 | | |
| | | 0.9935 | $AST_{1\text{-}2}$ | $*\omega_{f1}+\omega_{SRS2}=\omega_{ASt1\text{-}2}$ | | ≈668 | | |
| | | 1.06415 | $\lambda_{f1}$ | $\omega_{f1}$ | – | | | |
| | | 1.1456 | $St_{1\text{-}2}$ | $\omega_{f1}-\omega_{SRS2}=\omega_{St1\text{-}2}$ | | ≈668 | | |
| | ≈*c*(*aa*)≈*c* (see Figure 8) | 0.6348 | $AST_{7\text{-}1}$ | $*\omega_{f1}+7\omega_{SRS1}=\omega_{ASt7\text{-}1}$ | ≈908 | | | |
| | | 0.6736 | $AST_{6\text{-}1}$ | $*\omega_{f1}+6\omega_{SRS1}=\omega_{ASt6\text{-}1}$ | ≈908 | | | |
| | | 0.6847 | $AST_{1\text{-}2}\{AST_{5\text{-}1}\}$ | $**[(\omega_{f1}+5\omega_{SRS1})+\omega_{SRS2}]=$ $=\omega_{ASt1\text{-}2\{ASt5\text{-}1\}}$ | ≈908 | ≈668 | | |
| | | 0.7054 | $St_{1\text{-}2}\{AST_{6\text{-}1}\}$ | $**[(\omega_{f1}+6\omega_{SRS1})-\omega_{SRS2}]=$ $=\omega_{St1\text{-}2\{ASt6\text{-}1\}}$ | ≈908 | ≈668 | | |
| | | 0.7175 | $AST_{5\text{-}1}$ | $*\omega_{f1}+5\omega_{SRS1}=\omega_{ASt5\text{-}1}$ | ≈908 | | | |
| | | 0.7301 | $AST_{1\text{-}2}\{AST_{4\text{-}1}\}$ | $**[(\omega_{f1}+4\omega_{SRS1})+\omega_{SRS2}]=$ $=\omega_{ASt1\text{-}2\{ASt4\text{-}1\}}$ | ≈908 | ≈668 | | |
| | | 0.7536 | $St_{1\text{-}2}\{AST_{5\text{-}1}\}$ | $**[(\omega_{f1}+5\omega_{SRS1})-\omega_{SRS2}]=$ $=\omega_{St1\text{-}2\{ASt5\text{-}1\}}$ | ≈908 | ≈668 | | |
| | | 0.7675 | $AST_{4\text{-}1}$ | $*\omega_{f1}+4\omega_{SRS1}=\omega_{ASt4\text{-}1}$ | ≈908 | | | |
| | | 0.7819 | $AST_{1\text{-}2}\{AST_{3\text{-}1}\}$ | $**[(\omega_{f1}+3\omega_{SRS1})+\omega_{SRS2}]=$ $=\omega_{ASt1\text{-}2\{ASt3\text{-}1\}}$ | ≈908 | ≈668 | | |
| | | 0.8090 | $St_{1\text{-}2}\{AST_{4\text{-}1}\}$ | $**[(\omega_{f1}+4\omega_{SRS1})-\omega_{SRS2}]=$ $=\omega_{St1\text{-}2\{ASt4\text{-}1\}}$ | ≈908 | ≈668 | | |
| | | 0.8250 | $AST_{3\text{-}1}$ | $*\omega_{f1}+3\omega_{SRS1}=\omega_{ASt3\text{-}1}$ | ≈908 | | | |
| | | 0.8417 | $AST_{1\text{-}2}\{AST_{2\text{-}1}\}$ | $**[(\omega_{f1}+2\omega_{SRS1})+\omega_{SRS2}]=$ $=\omega_{ASt1\text{-}2\{ASt2\text{-}1\}}$ | ≈908 | ≈668 | | |
| | | 0.8731 | $St_{1\text{-}2}\{AST_{3\text{-}1}\}$ | $**[(\omega_{f1}+3\omega_{SRS1})-\omega_{SRS2}]=$ $=\omega_{St1\text{-}2\{ASt3\text{-}1\}}$ | | | | |
| | | 0.8918 | $AST_{2\text{-}1}$ | $*\omega_{f1}+2\omega_{SRS1}=\omega_{ASt2\text{-}1}$ | ≈908 | | | |
| | | 0.9113 | $AST_{1\text{-}2}\{AST_{1\text{-}1}\}$ | $**[(\omega_{f1}+\omega_{SRS1})+\omega_{SRS2}]=$ $=\omega_{ASt1\text{-}2\{ASt1\text{-}1\}}$ | ≈908 | ≈668 | | |
| | | 0.9385 | $Y_3Al_5O_{12}:Nd^{3+}$ | Luminescence[f] | | | | |
| | | 0.9460 | | | | | | |
| | | 0.9483 | $St_{1\text{-}2}\{AST_{2\text{-}1}\}$ | $**[(\omega_{f1}+2\omega_{SRS1})-\omega_{SRS2}]=$ $=\omega_{St1\text{-}2\{ASt2\text{-}1\}}$ | ≈908 | ≈668 | | |
| | | 0.9704 | $AST_{1\text{-}1}$ | $*\omega_{f1}+\omega_{SRS1}=\omega_{ASt1\text{-}1}$ | ≈908 | | | |

(*Continued*)

**Table 3.** Continued.

| Pumping condition | $\chi^{(3)}$-nonlinear lasing components | | | | SRS-promoting vibration modes [$cm^{-1}$] | | | |
|---|---|---|---|---|---|---|---|---|
| $\lambda_f$ [μm] | Excitation geometry[a] | Wave-length[b] [μm] | Spectral line[c] | Attribution[d] | $\omega_{SRS1}$ | $\omega_{SRS2}$ | $\omega_{SRS3}$[e] | $\omega_{SRS4}$[e] |
| | | 0.9935 | $ASt_{1-2}$ | $*\omega_{f1}+\omega_{SRS2}=\omega_{ASt1-2}$ | | ≈668 | | |
| | | 1.06415 | $\lambda_{f1}$ | $\omega_{f1}$ | – | | | |
| | | 1.1456 | $St_{1-2}$ | $\omega_{f1}-\omega_{SRS2}=\omega_{St1-2}$ | | ≈668 | | |
| | | 1.1780 | $St_{1-1}$ | $\omega_{f1}-\omega_{SRS1}=\omega_{St1-1}$ | ≈908 | | | |
| $Ca_2GaSi_2O_7$ crystal | | | | | | | | |
| 0.53207 | $\approx b(aa)\approx b$ (see Figure 9a) | 0.5027 | $ASt_{2-2}$ | $*\omega_{f2}+2\omega_{SRS2}=\omega_{ASt2-2}$ | | ≈550 | | |
| | | 0.5170 | $ASt_{1-2}$ | $*\omega_{f2}+\omega_{SRS2}=\omega_{ASt1-2}$ | | ≈550 | | |
| | | 0.53207 | $\lambda_{f2}$ | $\omega_{f2}$ | – | | | |
| | | 0.5481 | $St_{1-2}$ | $\omega_{f2}-\omega_{SRS2}=\omega_{St1-2}$ | | ≈550 | | |
| | | 0.5652 | $St_{2-2}$ | $*\omega_{f2}-2\omega_{SRS2}=\omega_{St2-2}$ | | ≈550 | | |
| | $a(cc)a$ (see Figure 9b) | 0.4942 | $ASt_{2-1}$ | $*\omega_{f2}+2\omega_{SRS1}=\omega_{ASt2-1}$ | ≈720 | | | |
| | | 0.5124 | $ASt_{1-1}$ | $*\omega_{f2}+\omega_{SRS1}=\omega_{ASt1-1}$ | ≈720 | | | |
| | | 0.53207 | $\lambda_{f2}$ | $\omega_{f2}$ | – | | | |
| | | 0.5533 | $St_{1-1}$ | $\omega_{f2}-\omega_{SRS1}=\omega_{St1-1}$ | ≈720 | | | |
| | | 0.5762 | $St_{2-1}$ | $*\omega_{f2}-2\omega_{SRS1}=\omega_{St2-1}$ | ≈720 | | | |
| | $c(aa)c$ (see Figure 10) | 0.4772 | $ASt_{3-1}$ | $*\omega_{f2}+3\omega_{SRS1}=\omega_{ASt3-1}$ | ≈720 | | | |
| | | 0.4942 | $ASt_{2-1}$ | $*\omega_{f2}+2\omega_{SRS1}=\omega_{ASt2-1}$ | ≈720 | | | |
| | | 0.4984 | $ASt_{1-4}$ | $**\omega_{f2}+\omega_{SRS4}=\omega_{ASt1-4}$ | | | | ≈1270 |
| | | 0.5027 | $ASt_{2-2}$ | $*\omega_{f2}+2\omega_{SRS2}=\omega_{ASt2-2}$ | | ≈550 | | |
| | | 0.5080 | $ASt_{1-3}\{ASt_{1-1}\}$ | $**[(\omega_{f2}+\omega_{SRS1})+\omega_{SRS3}]=$ $=\omega_{ASt1-3\{ASt1-1\}}$ | ≈720 | | ≈170 | |
| | | 0.5124 | $ASt_{1-1}$ | $*\omega_{f2}+\omega_{SRS1}=\omega_{ASt1-1}$ | ≈720 | | | |
| | | 0.5170 | $ASt_{1-2}$ | $*\omega_{f2}+\omega_{SRS2}=\omega_{ASt1-2}$ | | ≈550 | | |
| | | 0.5215 | $St_{1-3}\{ASt_{1-2}\}$ | $**[(\omega_{f2}+\omega_{SRS2})-\omega_{SRS3}]=$ $=\omega_{St1-3\{ASt1-2\}}$ | | ≈550 | ≈170 | |
| | | 0.5273 | $ASt_{1-3}$ | $*\omega_{f2}+\omega_{SRS3}=\omega_{ASt1-3}$ | | | ≈170 | |
| | | 0.53207 | $\lambda_{f2}$ | $\omega_{f2}$ | – | | | |
| | | 0.5369 | $St_{1-3}$ | $**\omega_{f2}-\omega_{SRS3}=\omega_{St1-3}$ | | | ≈170 | |
| | | 0.5431 | $ASt_{1-3}\{St_{1-2}\}$ | $**[(\omega_{f2}-\omega_{SRS2})+\omega_{SRS3}]=$ $=\omega_{St1-3\{St1-2\}}$ | | ≈550 | ≈170 | |
| | | 0.5481 | $St_{1-2}$ | $\omega_{f2}-\omega_{SRS2}=\omega_{St1-2}$ | | ≈550 | | |
| | | 0.5533 | $St_{1-1}$ | $\omega_{f2}-\omega_{SRS1}=\omega_{St1-1}$ | ≈720 | | | |
| | | 0.5585 | $St_{1-3}\{St_{1-1}\}$ | $**[(\omega_{f2}-\omega_{SRS1})-\omega_{SRS3}]=$ $=\omega_{St1-3\{St1-1\}}$ | ≈720 | | ≈170 | |
| | | 0.5652 | $St_{2-2}$ | $*\omega_{f2}-2\omega_{SRS2}=\omega_{St2-2}$ | | ≈550 | | |
| | | 0.5706 | $St_{1-4}$ | $**\omega_{f2}-\omega_{SRS4}=\omega_{St1-4}$ | | | | ≈1270 |
| | | 0.5762 | $St_{2-1}$ | $*\omega_{f2}-2\omega_{SRS1}=\omega_{St2-1}$ | ≈720 | | | |

[a] Notation is used in analogy to that in ref. [42]. The characters between parentheses are (from left to right) the polarization of the pump and of the nonlinear radiation, respectively, while the characters to the left and to the right of the parentheses are the propagation direction of the pump and the nonlinear radiation, respectively [b] Measurement accuracy is ±0.0003 μm [c] For example: $ASt_{1-3}\{ASt_{1-1}\}$ for $Ca_2MgSi_2O_7$ crystal: RFWM involving the first-order anti-Stokes component related to the vibrational mode $\omega_{SRS3} \approx 240\ cm^{-1}$ and the third-order anti-Stokes component related to the vibrational mode $\omega_{SRS1} \approx 908\ cm^{-1}$; $St_{1-3}\{St_{1-1}\}$ for $Ca_2Ga_2SiO_7$ crystal: the first-order Stokes component related to the vibrational mode $\omega_{SRS3} \approx 170\ cm^{-1}$ which has been originated from the first-order Stokes component related to the vibrational mode $\omega_{SRS1} \approx 720\ cm^{-1}$ [d] In square brackets, the most probable nonlinear optical generation process (SRS or RFWM) and the participating spectral components are given. Lines related to the cascaded and cross-cascaded $\chi^{(3)}$-nonlinear transitions are single- (*) and double- (**) asterisked, respectively [e] Two vibrational modes, $\omega_{SRS3} \approx 240\ cm^{-1}$ and $\omega_{SRS4} \approx 1576\ cm^{-1}$, of the $Ca_2MgSi_2O_7$ crystal and two vibrational modes, $\omega_{SRS3} \approx 170\ cm^{-1}$ and $\omega_{SRS4} \approx 1270\ cm^{-1}$, of the $Ca_2Ga_2SiO_7$ crystal are considered as combined vibrational modes. We refer to them as "phantom" or "masked" modes since they do not appear in the spontaneous Raman scattering spectra (see ref. [46] for $Ca_2MgSi_2O_7$). We hypothesize that they are the result of the cross-cascaded interactions between the coherently excited "original" phonons $\omega_{SRS1} \approx 908\ cm^{-1}$ and $\omega_{SRS2} \approx 668\ cm^{-1}$ for the $Ca_2MgSi_2O_7$ crystal: $\omega_{SRS1}(\approx 908\ cm^{-1}) - \omega_{SRS2}(\approx 668\ cm^{-1}) = \omega_{SRS3}(\approx 240\ cm^{-1})$, and $\omega_{SRS1}(\approx 908\ cm^{-1}) + \omega_{SRS2}(\approx 668\ cm^{-1}) = \omega_{SRS4}(\approx 1576\ cm^{-1})$. Likewise for the $Ca_2Ga_2SiO_7$ crystal: $\omega_{SRS1}(\approx 720\ cm^{-1}) - \omega_{SRS2}(\approx 550\ cm^{-1}) = \omega_{SRS3}(\approx 170\ cm^{-1})$, and $\omega_{SRS1}(\approx 720\ cm^{-1}) + \omega_{SRS2}(\approx 550\ cm^{1}) = \omega_{SRS4}(\approx 1270\ cm^{-1})$. Note that the presence of "combined" vibrational modes related to cross-cascaded $\chi^{(3)}$-nonlinear-optical interaction has already been observed previously in several crystals (see, e.g., refs. [9,40,43,44]) [f] The lines at 0.9385 and 0.9460 μm wavelength are caused by the emission from the $Nd^{3+}$:$Y_3Al_5O_{12}$ pump laser amplifier being incident on the monochromator and detector. They correspond to two $Nd^{3+}$-ion luminescence inter-Stark transitions at 11 507 $cm^{-1}$ $^4F_{3/2} \rightarrow {}^4I_{9/2}$ 852 and 11 423 $cm^{-1}$ $^4F_{3/2} \rightarrow {}^4I_{9/2}$ 852 $cm^{-1}$, respectively (see, e.g., ref. [45]). The spectral lines could be used as reference lines.

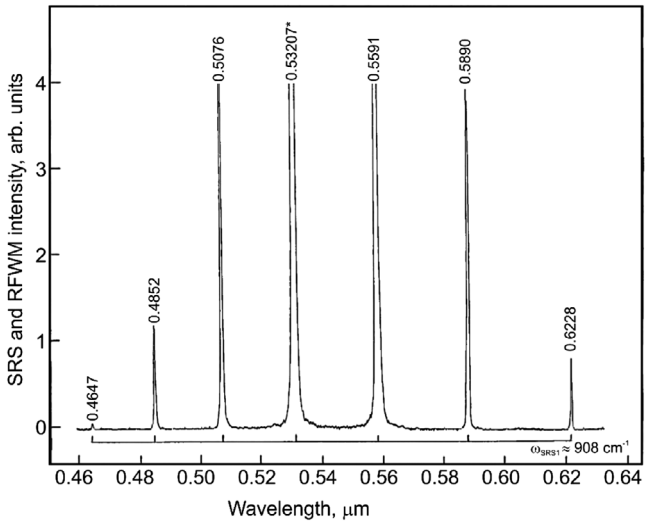


**Figure 4.** SRS and RFWM spectrum of the tetragonal $Ca_2MgSi_2O_7$ crystal recorded with picosecond pumping at the wavelength $\lambda_{f2} = 0.53207$ μm in excitation geometry *a*(*cc*)*a*. The wavelength of all lines (pump line is asterisked) are given in μm, their intensities are shown without correction for the sensitivity of the used multichannel analyzing system with a Si-CCD line sensor (Hamamatsu, model S3924-1024Q). The energy spacing related to the SRS-promoting vibrational mode $\omega_{SRS1} \approx 908$ cm$^{-1}$ of the Stokes and anti-Stokes sidebands is indicated by the horizontal scale brackets. The assignment of all recorded spectral lines is given in Table 3.

same M and $T^{(2)}$ cations given). So, while the Zn compound $Ca_2ZnSi_2O_7$ is uniaxial negative with small birefringence $n_e - n_o$ around −0.012[47] $Ca_2MgSi_2O_7$ is uniaxial positive with a rather small birefringence $n_e - n_o$ around +0.008, and the refractive indices of both compounds do not allow phase matching for, e.g., SHG. In contrast, the refractive indices of germanate melilites with M = Ba, Sr and $T^{(1)}$ = Mg show larger birefringence of up to 0.04 and phase-matched SHG and SFG is possible in a broad wavelength range. This difference also affects the observed SRS and RFWM spectra of melilite-type crystals, where cross-cascaded $\chi^{(3)} \leftrightarrow \chi^{(2)}$-processes are observed for $Ba_2MgGe_2O_7$, $Ba_2ZnGe_2O_7$, and $Sr_2MgGe_2O_7$ (see Table 1), but not for $Ca_2ZnSi_2O_7$ and $Ca_2MgSi_2O_7$. On the other hand, however, cross-cascaded $\chi^{(3)} \leftrightarrow \chi^{(3)}$-processes are observed in the latter two crystals due to the presence of several SRS-promotoing vibration modes.

## 5. Conclusion

The current work extends our investigations during the preceding decade of new SRS-active non-centrosymmetric tetragonal ($P\bar{4}2m - D_{2d}^3$) melilite-type crystals (among which the first crystal was $Ba_2MgGe_2O_7$,[4] see Table 1). As can be seen from the overview in Table 1 most of these crystals, including the two melilites of the present work, $Ca_2MgSi_2O_7$ and $Ca_2Ga_2SiO_7$, are $Ln^{3+}$(here, $Nd^{3+}$)-laser active media. Together with the here discovered attractive SRS properties of $Ca_2MgSi_2O_7$ and $Ca_2Ga_2SiO_7$, this allows a simultaneous functionality as a host for laser ions and as a Raman-shifting material, which opens the possibility to realize self-SRS-laser converters. The development of such lasers is currently of great interest in modern laser physics as it allows for the generation of novel laser sources at wavelengths which are not directly accessible with conventional laser materials. With the two crystals of the present work the currently available panoply of self-SRS-laser converter materials could be complemented. An overview of so far known crystalline self-SRS media is given in Table S1 (Supporting Information).

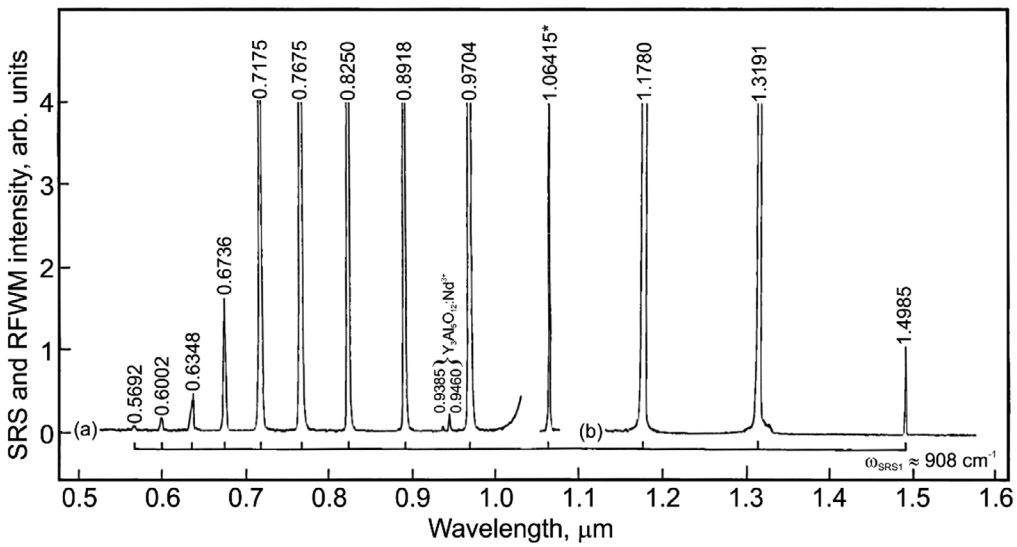


**Figure 5.** Two parts of the SRS and RFWM spectrum of the tetragonal $Ca_2MgSi_2O_7$ crystal recorded with picosecond pumping at the wavelength $\lambda_{f1} = 1.06415$ μm in excitation geometry *a*(*cc*)*a*. Part (a) was recorded with a Si-CCD line sensor (Hamamatsu, model S3924-1024Q) and part (b) with an InGaAs-CMOS line sensor (Hamamatsu, model G9204-512D), see the corresponding spectral sensitivity in Figure 3b). The energy spacing related to the SRS-promoting vibrational mode $\omega_{SRS1} \approx 908$ cm$^{-1}$ of the Stokes and anti-Stokes sidebands is indicated by the horizontal scale brackets. The assignment of all recorded spectral lines is given in Table 3.

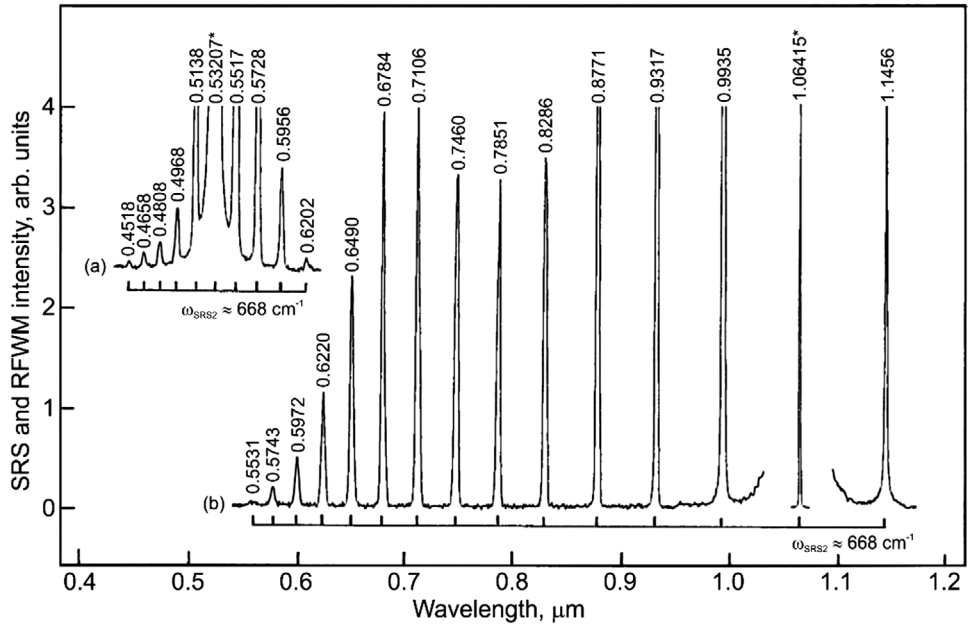


**Figure 6.** SRS and RFWM spectra of the tetragonal $Ca_2MgSi_2O_7$ crystal recorded in excitation geometry $\approx b(aa)\approx b$ with picosecond pumping at the wavelengths a) $\lambda_{f2} = 0.53207$ μm and b) $\lambda_{f1} = 1.06415$ μm, using Si-CCD and InGaAs-CMOS line Hamamatsu sensors (see Figure 3). The energy spacing of recorded Stokes and anti-Stokes sidebands are related to SRS-promoting vibrational mode $\omega_{SRS2} \approx 668$ cm$^{-1}$ is indicated by the horizontal scale brackets. The used notations are analogous to that of Figure 4. The assignment of all recorded spectral lines is given in Table 3.

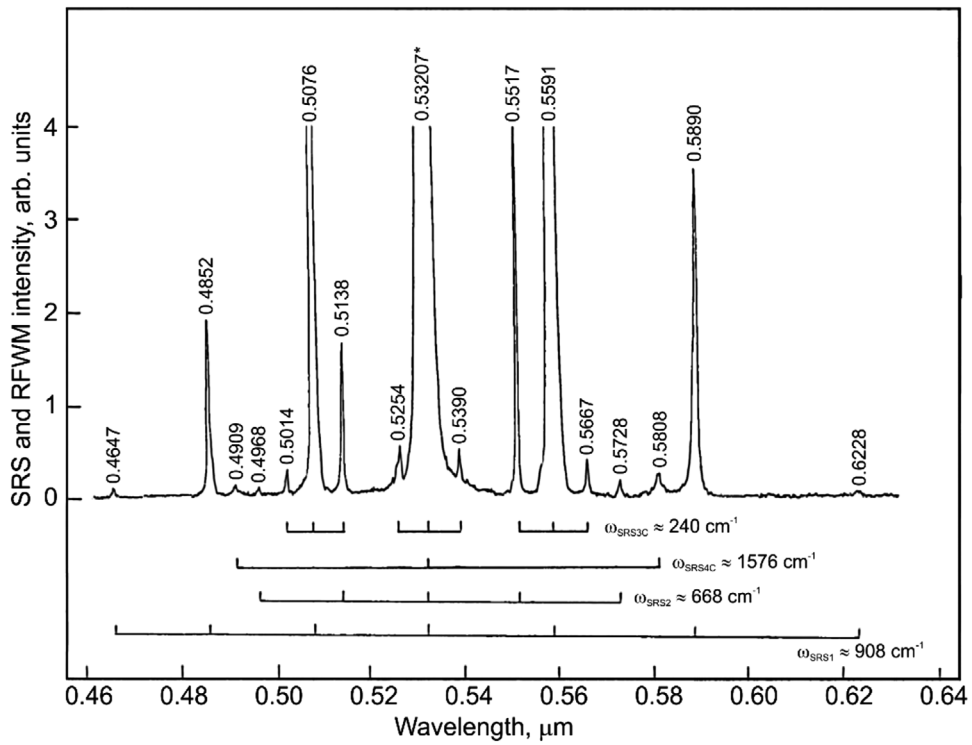


**Figure 7.** SRS and RFWM spectrum of the tetragonal $Ca_2MgSi_2O_7$ crystal recorded with picosecond pumping at the wavelength $\lambda_{f2} = 0.53207$ μm in excitation geometry $c(aa)c$ using a Si-CCD line sensor (Hamamatsu, model S3924-1024Q). The energy spacing related to the SRS-promoting vibrational modes $\omega_{SRS1} \approx 908$ cm$^{-1}$, $\omega_{SRS2} \approx 668$ cm$^{-1}$, $\omega_{SRS3C} \approx 240$ cm$^{-1}$, and $\omega_{SRS4C} \approx 1576$ cm$^{-1}$ of the Stokes and anti-Stokes sidebands is indicated by the horizontal scale brackets. The used notations are analogous to that of Figure 4. The assignment of all recorded spectral lines is given in Table 3. Note that this spectrum is also given in ref. [21], however, with a reduced wavelength range.

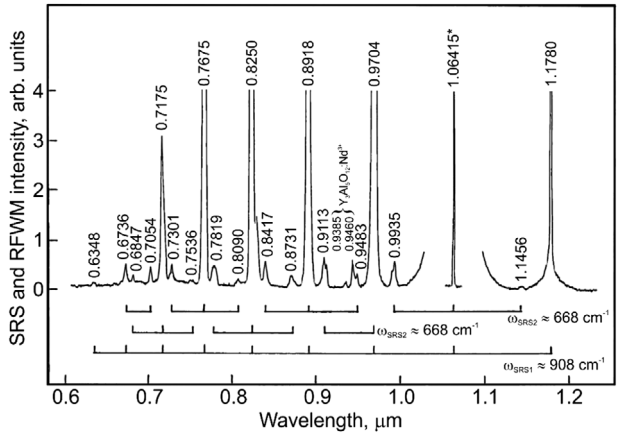


**Figure 8.** SRS and RFWM spectrum of the tetragonal $Ca_2MgSi_2O_7$ crystal recorded with picosecond pumping at the wavelength $\lambda_{f1} = 1.06415$ μm in excitation geometry $\approx c(aa)\approx c$ using a Si-CCD line sensor (Hamamatsu, model S3924-1024Q). The energy spacing related to the SRS-promoting vibrational modes $\omega_{SRS1} \approx 908$ cm$^{-1}$ and $\omega_{SRS2} \approx 668$ cm$^{-1}$ of the Stokes and anti-Stokes sidebands is indicated by the horizontal scale brackets. The used notations are analogous to the in Figure 4. The assignment of all recorded spectral lines is given in Table 3.

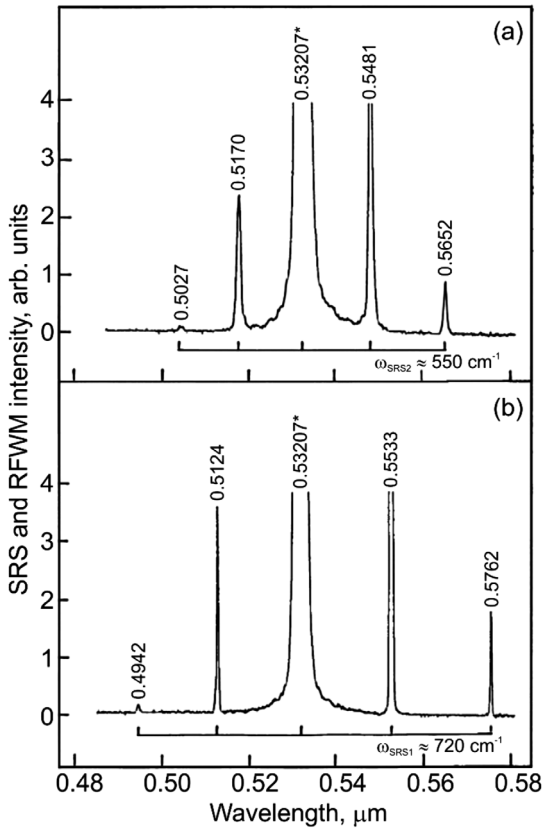


**Figure 9.** SRS and RFWM spectra of the tetragonal $Ca_2Ga_2SiO_7$ crystal recorded with picosecond pumping at the wavelength $\lambda_{f2} = 0.53207$ μm in excitation geometry: a) $\approx b(aa)\approx b$ and b) $a(cc)a$ with a Si-CCD line sensor (Hamamatsu, model S3924-1024Q). The energy spacing related to the SRS-promoting vibrational modes: a) $\omega_{SRS2} \approx 550$ cm$^{-1}$ and b) $\omega_{SRS1} \approx 720$ cm$^{-1}$ of the Stokes and anti-Stokes sidebands is indicated by the horizontal scale brackets. The used notations are analogous to that of Figure 4. The assignment of all recorded spectral lines is given in Table 3.

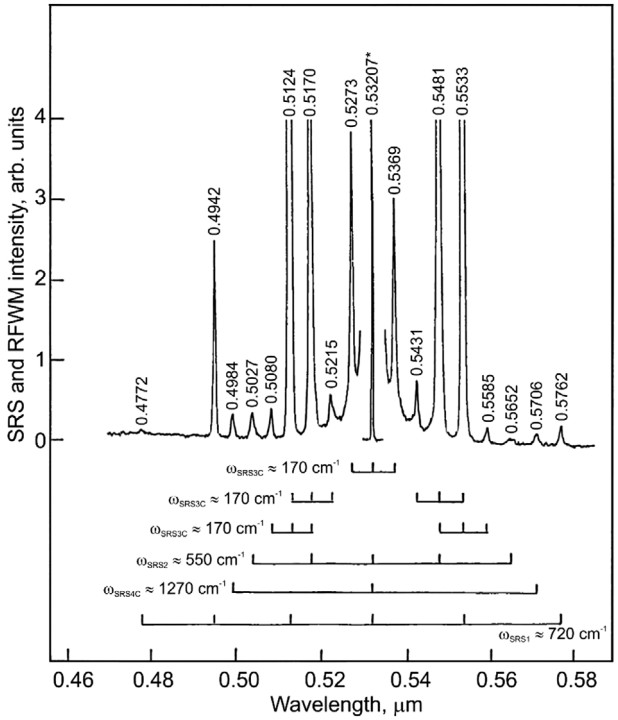


**Figure 10.** SRS and RFWM spectrum of the tetragonal $Ca_2Ga_2SiO_7$ crystal recorded with picosecond pumping at the wavelength $\lambda_{f2} = 0.53207$ μm in excitation geometry $c(aa)c$ using a Si-CCD line sensor (Hamamatsu, model S3924-1024Q). The energy spacing related to the SRS-promoting vibrational modes $\omega_{SRS1} \approx 720$ cm$^{-1}$, $\omega_{SRS2} \approx 550$ cm$^{-1}$, $\omega_{SRS3C} \approx 170$ cm$^{-1}$, and $\omega_{SRS4C} \approx 1270$ cm$^{-1}$ of the Stokes and anti-Stokes sidebands is indicated by the horizontal scale brackets. The used notations are analogous to that of Figure 4. The assignment of all recorded spectral lines is given in Table 3.

## Supporting Information

Supporting Information is available from the Wiley Online Library or from the author.

## Acknowledgements

The authors wish to note that the investigations were considerably promoted through mutual scientific help within the "Joint Open Laboratory for Laser Crystals and Precise Laser Systems," and were stimulated by fundamental research programs of the Institute of Crystallography, Federal Research Center of "Crystallography and Photonics" of the Russian Academy of Sciences, by the Institute of Optics and Atomic Physics of the Technical University of Berlin and by the Section Crystallography, Institute of Geology and Mineralogy of the University of Cologne. The authors dedicate this manuscript to the memory of their colleague and friend, Prof. Alexander A. Kaminskii, who passed away on October 29th, 2019. The authors are grateful for his tremendous contributions to the study of stimulated Raman scattering and other nonlinear optical effects in various crystals over the past three decades.

## Conflict of Interest

The authors declare no conflict of interest.

## Keywords

$Ca_2Ga_2SiO_7$, $Ca_2MgSi_2O_7$, many-phonon $\chi^{(3)}$-nonlinear lasing, stimulated Raman scattering (SRS), tetragonal melilite-type crystals

Received: February 21, 2020
Revised: April 21, 2020
Published online: June 14, 2020

[1] M. Alam, K. H. Gooen, B. Di Bartolo, A. Linz, E. Sharp, L. Gillespie, G. Janney, *J. Appl. Phys.* **1968**, *39*, 4728.
[2] M. J. Weber, *Handbook of Laser Wavelengths*, CRC Press, Boca Raton, FL **2000**.
[3] A. A. Kaminskii, *Laser Photonics Rev.* **2007**, *1*, 93.
[4] A. A. Kaminskii, L. Bohatý, P. Becker, J. Liebertz, P. Held, H. J. Eichler, H. Rhee, J. Hanuza, *Laser Phys. Lett.* **2008**, *5*, 845.
[5] A. A. Kaminskii, L. Bohatý, P. Becker, J. Liebertz, H. J. Eichler, H. Rhee, J. Hanuza, *Laser Phys. Lett.* **2010**, *7*, 528.
[6] P. Becker, L. Bohatý, J. Liebertz, H.-J. Kleebe, M. Müller, H. J. Eichler, H. Rhee, J. Hanuza, A. A. Kaminskii, *Laser Phys. Lett.* **2010**, *7*, 367.
[7] D. J. Horowitz, L. F. Gillespie, J. E. Miller, E. J. Sharp, *J. Appl. Phys.* **1972**, *43*, 3527.
[8] T. H. Allik, M. J. Ferry, R. J. Reeves, R. C. Powell, W. W. Hovis, D. P. Caffey, R. A. Utano, L. Merkle, C. F. Campana, *J. Opt. Soc. Am. B* **1990**, *7*, 1190.
[9] A. A. Kaminskii, H. Rhee, O. Lux, H. J. Eichler, L. Bohatý, P. Becker, J. Liebertz, K. Ueda, A. Shirakawa, V. V. Koltashev, J. Hanuza, J. Dong, D. B. Stavrovskii, *Laser Phys. Lett.* **2011**, *8*, 859.
[10] A. A. Kaminskii, H. H. Yu, J. Y. Wang, Y. Y. Zhang, H. J. Zhang, O. Lux, H. Rhee, H. J. Eichler, J. Hanuza, H. Yoneda, A. Shirakawa, *Laser Phys.* **2014**, *24*, 085803.
[11] W. Ryba-Romanowski, S. Goląb, G. Dominiak-Dzik, M. Berkowski, *Mater. Sci. Eng., B* **1992**, *15*, 217.
[12] M. Malinowski, I. Pracka, B. Surma, T. Łukasiewicz, W. Woliński, R. Wolski, *Opt. Mater.* **1996**, *6*, 305.
[13] F. Hanson, D. Dick, H. R. Verdun, M. Kokta, *J. Opt. Soc. Am. B* **1991**, *8*, 1668.
[14] A. A. Kaminskii, E. L. Belokoneva, B. V. Mill, S. E. Sarkisov, K. Kurbanov, *Phys. Status Solidi A* **1986**, *97*, 279.
[15] A. A. Kaminskii, E. L. Belokoneva, B. V. Mill', S. A. Tamazyan, K. Kurbanov, *Inorg. Mater.* **1986**, *22*, 993.
[16] A. A. Kaminskii, H. R. Verdun, B. V. Mill, *Phys. Status Solidi A* **1992**, *129*, K125.
[17] A. A. Kaminskii, V. A. Karasev, V. D. Dubrov, V. P. Yakunin, B. V. Mill, A. V. Butashin, *Sov. J. Quantum Electron.* **1992**, *22*, 97.
[18] A. A. Kaminskii, M. I. Demchuk, N. V. Zhavoronkov, V. P. Michailov, *Phys. Status Solidi A* **1989**, *113*, K257.
[19] A. A. Kaminskii, H. Nakao, A. Shirakawa, K. Ueda, J. Liebertz, P. Becker, L. Bohatý, *Appl. Phys. B* **2011**, *103*, 629.
[20] H. Rhee, *Ph.D. Thesis*, Technical University Berlin, **2012**.
[21] A. A. Kaminskii, *Dokl. Phys.* **2019**, *64*, 313.
[22] F. Röthlisberger, F. Seifert, M. Czank, *Eur. J. Mineral.* **1990**, *2*, 585.
[23] E. Burzo, in *Melilites and Related Silicates*, Landolt-Börnstein – Group III: Condensed Matter, Vol. 27I2 (Ed: H. P. J. Wijn), Springer, Berlin **2005**.
[24] B. E. Warren, *Z. Kristallogr.* **1930**, *74*, 131.
[25] K. Kusaka, K. Hagiya, M. Ohmasa, Y. Okano, M. Mukai, K. Iishi, N. Haga, *Phys. Chem. Miner.* **2001**, *28*, 150.
[26] B. S. Hemingway, H. T. Evans, G. L. Nord, H. T. Haselton, R. A. Robie, J. J. McGee, *Can. Mineral.* **1986**, *24*, 425.
[27] F. Seifert, M. Czank, B. Simons, W. Schmahl, *Phys. Chem. Miner.* **1987**, *14*, 26.
[28] L. Bindi, P. Bonazzi, M. Dušek, V. Petříček, G. Chapuis, *Acta Crystallogr., Sect. B: Struct. Sci.* **2001**, *57*, 739.
[29] B. Bagautdinov, K. Hagiya, S. Noguchi, M. Ohmasa, N. Ikeda, K. Kusaka, K. Iishi, *Phys. Chem. Miner.* **2002**, *29*, 346.
[30] Z. Burshtein, Y. Shimony, I. Levy, A. M. Lejus, J. M. Benitez, F. Mougel, *J. Opt. Soc. B* **1996**, *13*, 1941.
[31] L. Bohatý, J. Liebertz, *Z. Kristallogr.* **1982**, *159*, 277.
[32] R. D. Shannon, R. C. Shannon, O. Medenbach, R. X. Fischer, *J. Phys. Chem.* **2002**, *31*, 931.
[33] P. Becker, P. Held, J. Liebertz, L. Bohatý, *Cryst. Res. Technol.* **2009**, *44*, 603.
[34] K. P. Birch, M. J. Downs, *Metrologia* **1994**, *31*, 315.
[35] E. M. Levin, C. R. Robbins, H. F. McMurdie, in *Phase Diagrams for Ceramists* (Ed: M. K. Reser), The American Ceramic Society, Columbus, OH **1985**.
[36] C. B. Finch, G. W. Clark, L. A. Harris, C. S. Yust, *J. Cryst. Growth* **1974**, *23*, 295.
[37] J. Liebertz, S. Stähr, *Z. Kristallogr.* **1982**, *159*, 271.
[38] J. W. Anthony, R. A. Bideaux, K. W. Bladh, N. C. Nichols, *Handbook of Mineralogy*, Mineral Data Publishing, Tucson, AZ **1990**.
[39] Z. Burshtein, Y. Kostoulas, H. M. van Driel, *J. Opt. Soc. Am. B* **1997**, *14*, 2477.
[40] A. A. Kaminskii, O. Lux, H. Rhee, A. Kaltenbach, H. J. Eichler, J. Zhang, D. Y. Tang, H. Yu, H. Zhang, J. Wang, H. Yoneda, K. Ueda, A. Shirakawa, *Phys. Status Solidi B* **2014**, *251*, 1045.
[41] A. A. Kaminskii, O. Lux, H. Rhee, H. J. Eichler, H. Yoneda, A. Shirakawa, K. Ueda, R. Rückamp, L. Bohatý, P. Becker, *Laser Phys. Lett.* **2013**, *10*, 073001.
[42] T. C. Damen, S. P. S. Porto, B. Tell, *Phys. Rev.* **1966**, *142*, 570.
[43] A. A. Kaminskii, O. Lux, J. Hanuza, H. Rhee, H. J. Eichler, H. Yoneda, J. Zhang, D. Tang, A. Shirakawa, *Laser Photonics Rev.* **2014**, *8*, 904.
[44] A. A. Kaminskii, H. Yu, H. Zhang, J. Wang, O. Lux, H. Rhee, H. J. Eichler, H. Yoneda, A. Shirakawa, J. Zhang, G. Tang, *Laser Phys.* **2014**, *24*, 125803.
[45] A. A. Kaminskii, *Laser Crystal: Their Physics and Properties*, Springer, Berlin **1981**.
[46] J. Hanuza, M. Ptak, M. Mączka, K. Hermanowicz, J. Lorenc, A. A. Kaminskii, *J. Solid State Chem.* **2012**, *191*, 90.
[47] P. Becker, E. Libowitzky, L. Bohatý, J. Liebertz, H. Rhee, H. J. Eichler, A. A. Kaminskii, *Phys. Status Solidi A* **2012**, *209*, 327.